1 **Triggering effects of large topography and boundary layer turbulence over the**
2 **Tibetan Plateau on convection**

3 **Xiangde Xu[1], Yi Tang[1,2], Yinjun Wang[1], Hongshen Zhang[3] and Mingyu Zhou[4]**

5 [1] State Key Laboratory of Severe Weather, Chinese Academy of Meteorological
6 Sciences, Beijing, China.

7 [2] School of Environmental Studies, China University of Geosciences, Wuhan, China.

8 [3] Peking University, Beijing, China

9 [4] National Marine Environmental Forecasting Center, Beijing, China

11 Corresponding author: Yinjun Wang (pbl_wyj@sina.cn) and Hongshen Zhang
12 (hsdq@pku.edu.cn)

13 **Abstract**

14   In this study, we analyze the diurnal variations and formation mechanism of low
15 clouds at different elevations. We further discuss whether there exist triggering
16 mechanism for convection over the Tibetan Plateau (TP), and whether there is an
17 association among low air density, strong turbulence and ubiquitous "popcorn-like"
18 cumulus clouds. The buoyancy term (BT) and shear term (ST) over the TP are
19 significantly greater than those at the low elevation, which is favorable for the
20 formation of increasing planetary boundary layer height (PBLH), and also plays a key
21 role in the convective activities in the lower troposphere. The lifting condensation
22 level (LCL) increases with the increasing of PBLH-LCL over the TP. From the
23 viewpoint of global effects, the triggering effects of the dynamical structure within the
24 boundary layer on convective clouds in the northern hemisphere are analyzed. There
25 are strong ST and BT at two high elevation regions (TP and Rocky Mountains), and
26 the strong thermal turbulence results in obvious positive value of PBLH-LCL at high
27 elevation regions under low RH condition in the northern hemisphere. The values of
28 PBLH-LCL slightly greater than zero correspond spatially to more low cloud cover
29 (LCC) in the central part of Rocky Mountains, but obvious large-scale subsidence on
30 both sides of the mountain leads to strong inversion above PBL and lower RH in PBL,
31 which further lead to less LCC in these areas. Thus   less LCC is generated at Rocky
32 Mountains compared to the TP.

33 **Introduction**

34   The Tibetan Plateau (TP), which resembles a "third pole" and a "world water
35 tower", plays an important and special role in the global climate and energy–water

36 cycle (Xu et al., 2008; Wu et al., 2015). The TP covers a quarter of China.
37 Additionally, the average altitude of the TP is 4000 meters, reaching 1/3 of the
38 tropopause height, so it is called the "World Roof". Cumulus convection over the TP
39 transfers heat, moisture and momentum into the free troposphere, which can impact
40 the atmospheric circulation regionally and globally (Li and Zhang, 2016; Xu et al.,
41 2014) and reveals the important "window effect" for the transfer and exchange of
42 global energy and water vapor over the TP. The special heat source dynamic effect
43 constitutes the "window effect" and "thermally driven" mechanism over the TP.

44 The results of the TIPEX II, which was carried out in 1998, showed that the strong
45 convective plumes within PBL observed by sodar and a frequently occurred deep
46 mixed layer (>2 km) can lead to ubiquitous "popcorn‐like" cumulus clouds in
47 Dangxiong, and Xu et al. (2002) proposed a comprehensive physical pattern of
48 land-air dynamic and thermal structure on the Qinghai-Xizang Plateau (Xu et al.,
49 2002; Zhou, 2000). The previous studies have done many valuable researches on the
50 triggering mechanism of moist convection over moist and dry surfaces based on
51 atmospheric observations and simulations (Ek and Mahrt, 1994; Findell and Eltahir,
52 2003; Gentine et al., 2013). For dry surface, the weak stratification and strong
53 sensible heat flux result in the rapid growth of PBLH so that the relative humidity at
54 the top of the boundary layer RH_{top} decreases rapidly, which favors the formation of
55 clouds. For moist surface, strong stratification and evaporation (small bowen ratio)
56 result in slow growth of PBLH, also increase the mixed layer specific humidity and
57 RH_{top}, which favor the formation and development of clouds. Taylor et al. (2012)
58 found that the afternoon rain falls preferentially over soils that are relatively dry
59 compared to the surrounding area, especially for semi-arid regions. Guillod et al.
60 (2015) reconciled spatial and temporal soil moisture effects on the afternoon rainfall.
61 They showed that afternoon precipitation events tend to occur during wet and
62 heterogeneous soil moisture conditions, while being located over comparatively drier
63 patches. Tuttle et al. (2016) showed the empirical evidence of contrasting soil
64 moisture–precipitation feedbacks across the United States, and they found that soil
65 moisture anomalies significantly influence rainfall probabilities over 38% of the area
66 with a median factor of 13%. According to the model results over dry and wet soils in
67 Illinois, Findell et al. (2003) summarized the predictive capability of rain and shallow
68 clouds gained from use of the convective triggering potential (CTP) and a low-level
69 humidity index, HI_{low} as measures of the early morning atmospheric setting. Our
70 previous studies pointed out that the developments of these cumulus clouds are related
71 to the special large scale dynamic structure and turbulence within PBL over the TP
72 (Xu et al., 2014; Wang et al., 2020). All the above results indicate the topography of
73 the TP plays a major role in increasing the occurrence frequency of the strong
74 convective clouds (Luo et al., 2011). This conclusion is consistent with the viewpoint
75 of Flohn (1967) who emphasized the chimney effect of the huge cumulonimbus
76 clouds on heat transfer in the upper troposphere.
77 The TP is one of the regions in China where high frequency of cumulus clouds
78 occurs, and the development of cumulus system is related to both the turbulence and

79 special dynamical structure in PBL over the TP. The vertical motion over the TP is
80 associated with the anomalous convective activities. However, as Li and Zhang (2016)
81 mentioned, the details of PBL process are not very clear, and also the diurnal
82 variations and formation mechanism of low clouds over the TP and low elevation
83 regions are still not very clear. The different variation characteristics of these low
84 clouds at different elevations also need to be discussed and analyzed. We further need
85 to discuss whether there exist "high efficiency" triggering mechanisms for convection
86 over the TP, and whether there is an association among low air density, strong
87 turbulence and ubiquitous "popcorn-like" cumulus clouds. Is there also strong
88 turbulence at higher elevation region with lower air density in the globe? Because
89 both the TP and Rocky Mountains are   high elevation regions with huge area in
90 mid-latitude, in this study we mainly focus on these two regions to analyze the above
91 scientific questions.

92 **2 Observational and reanalysis data**

93   We use in situ measurements of temperature (T) and relative humidity (RH) at 2 m
94 height, surface pressure data every hour, and low cloud cover (LCC) every three
95 hours from 2402 automatic weather stations   from June to August of 2010-2019 in
96 China. LCC here refers to the fraction of the sky obscured by low clouds as estimated
97 by human observers, including five cloud types: nimbostratus (Ns), stratocumulus
98 (Sc), stratus (St), cumulus (Cu), and deep convection (DC). These surface observation
99 datasets are provided by China National Meteorological Information Center.
100   In addition, we use the hourly 0.25° x 0.25° ERA5 reanalysis surface-layer data
101 in summer (June 1 to August 31) from 2010 to 2019 (Hersbach et al., 2020).
102   We use more than 4 years (from June 15 2006 to August 31 2010) of the satellite
103 (CloudSat radar and Calipso lidar)-merged cloud classification product
104 2B-CLDCLASS-lidar to calculate the mean LCC with 1°x1° resolution at about 2:00
105 pm and 2:00 am LT in summer. The introduction of this product and details of the
106 LCC calculation methods are summarized in Sassen and Wang (2008) and Wang et al
107 (2020).
108   We also use the 1 year (from June 1 to August 31 in 2016) geostationary satellite
109 himawari-8 retrieval product (cloud top height) over land in East Asia.
110   In this study, using ERA5 reanalysis data, we calculate the buoyancy term (BT)
111 ($g/\theta_v \overline{w'\theta'_v}$) and shear term (ST) ($-\partial\overline{u}/\partial z \overline{u'w'}$) in the TKE equation for each grid. Both
112 of these two terms can be used to analyze the effect of boundary layer turbulence in
113 surface layer on convection. The details of the method for computing BT and ST are
114 as follows:
115   The shear term (ST) ($-\partial\overline{u}/\partial z \overline{u'w'} - \partial\overline{v}/\partial z \overline{v'w'}$) and buoyancy term (BT) ($g/\theta_v \overline{w'\theta'_v}$)
116 in the TKE equation maintain the turbulent motions. In order to simplify calculations,
117 the x-axis is directed along the average wind. Assuming horizontal homogeneity and
118 no mean divergence, the TKE equation is written as

119 $$\frac{\partial \overline{e}}{\partial t} = \frac{g}{\theta_v}\overline{w'\theta'_v} - \overline{u'w'}\frac{\partial \overline{u}}{\partial z} - \frac{\partial \left(\overline{w'e}\right)}{\partial z} - \frac{1}{\overline{\rho}}\frac{\partial \left(\overline{w'p'}\right)}{\partial z} - \varepsilon.$$ (1)

120 The left side of eq. (1) is the local time variation $\partial \overline{e}/\partial t$, and the terms on the

121 right-hand side of eq. (1) describe the buoyancy and shear energy production or

122 consumption, turbulent transport of $\overline{e}$, pressure correlation and viscous dissipation

123 (Stull, 1988).

124 Here we use eq. (2) to calculate virtual potential temperature θ_v, and $\overline{w'\theta'_v}$ is

125 derived from eq. (3). Finally, we derive BT.

126 $$\theta_v = T\left(1 + 0.608q\right)\left(\frac{p_0}{p}\right)^{\frac{R}{c_p}},$$ (2)

127 $$H = \rho c_p \overline{w'\theta'_v},$$ (3)

128 Where g = 9.8 m s^{-2} is the gravitational constant, and H (W m^{-2}) is the sensible heat

129 flux, ρ (kg m^{-3}) is the air density, R is the specific gas constant for dry air, c$_p$ (=1004 J

130 kg^{-1} K^{-1}) is the specific heat of air at constant pressure, T is the air temperature at 2 m

131 heigh, q is the specific humidity at 2 m height, p_0 and p are standard atmospheric

132 pressure and surface pressure, respectively.

133 The $\partial \overline{u}/\partial z$ in the surface layer is estimated as

134 $$\frac{\partial \overline{u}}{\partial z} = \phi_m\left(\zeta\right)\frac{u_*}{kz},$$ (4)

135 and the non-dimensional wind profiles ϕ_m (Dyer, 1974) is :

136 $$\phi_m = 1 + 5\zeta, \left(\zeta > 0\right)$$ (5)

137 $$\phi_m = \left(1 - 16\zeta\right)^{-1/4}, \left(\zeta < 0\right)$$ (6)

138 $$\zeta = \frac{z}{L}, L = \frac{-u_*^3}{\kappa \frac{g}{\theta_v}\overline{w'\theta'}},$$ (7)

139 $$\tau = \sqrt{\tau_x^2 + \tau_y^2},$$ (8)

140 $$\tau = \rho u_*^2,$$ (9)

141 $$\tau = -\rho \overline{u'w'}.$$ (10)

142 Where the von Karman constant κ =0.4, and z = 10 m. $\overline{u}$ is the horizontal wind

143 speed at level z and u_* is the frictional velocity. The stability parameter z/L is defined

144   in eq. (7). τ_x and τ_y are the Eastward and Northward turbulent surface stress,

145   respectively. τ is turbulent fluxes of momentum, which can be calculated by using eq.

146   (8). Then we use eq. (9) to derive u_*. We also use eq. (10) to derive $-\overline{u'w'}$. Finally,

147   we derive ST.

148

149   3 Results

150   Figure 1 (a) shows the spatial distribution of over-land low cloud cover (LCC) in

151   China from June to August of 1951-2019 . The high value areas of LCC that present

152   in "ribbon pattern" are mainly located in the TP and Yangtze River Valley. Using four

153   years of CloudSat-Calipso satellite data, Li and Zhang (2016) also confirmed that the

154   climatological occurrence of cumulus over the TP is significantly greater than that in

155   mid-eastern China on the same latitude. The elevated land surface with strong

156   radiative heating makes the massive TP a favorable region for initiating convective

157   cells with a high frequency of cumulonimbus and mesoscale convective systems

158   (Sugimoto and Ueno, 2012). As a strong heat source, the TP has frequent convective

159   activities in summer. During the TIPEX Ⅱ in 1998, the long and narrow thermal

160   plume corresponding with vigorous cellular convection on micro-scale was observed

161   by sodar in Dangxiong. The convective plume and "raised" cloud over the TP are

162   probably related to the organized eddies on the meso-scale and micro-scale over the

163   TP.

164   As shown in Figure 2, in general, LCC increases with the increasing elevation.

165   The median of LCC_Hs are significantly greater than those of LCC_L and LCC_M

166   throughout the day. The diurnal variations of LCC_L and LCC_M are generally

167   distributed in unimodal pattern with the maximum appearing at 2:00 pm BT (median

168    $LCC_L = 37\%$, $LCC_M = 38\%$) and low values (~20%) are maintained during the night.

169   The diurnal variation of LCC_H presents a bimodal curve with the maximum appearing

170   at 5:00 pm BT (median $LCC_H = 69\%$) and the secondary local maximum appearing at

171   8:00 am BT (median $LCC_H = 61\%$). Compared to the low elevation, the interquartile

172   ranges (IQRs) of LCC_H are less than those of LCC_L and LCC_M, which imply the

173   LCC_H maintains high values during the day.
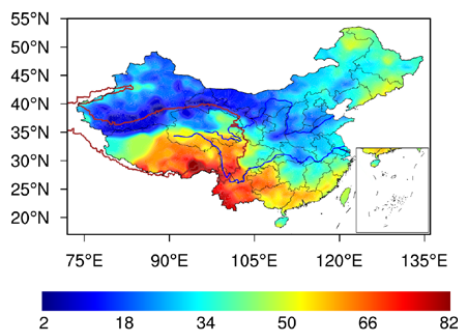
174

175   Figure 1. The monthly mean LCC derived from surface observations in summer from
176   1951 to 2019 in China.
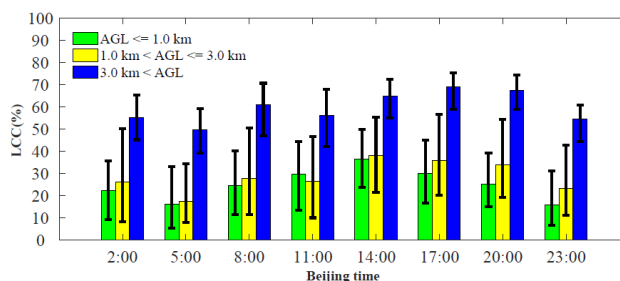
177

178   Figure 2. The durinal cycle of LCC in summer from 2010 to 2019 at different
179   elevations: ASL ≤ 1.0 km (LCC$_L$), 1.0 km < ASL ≤ 3.0 km (LCC$_M$), and 3.0 km <
180   ASL (LCC$_H$). It should be noted that all the sites are ranged from 27N to 40N in
181   China, and   each sample is derived from monthly mean LCC at a particular time in
182   summer for each site. The bar and error bar represent the median values and
183   interquartile ranges (IQRs) of LCC, respectively.

184

185
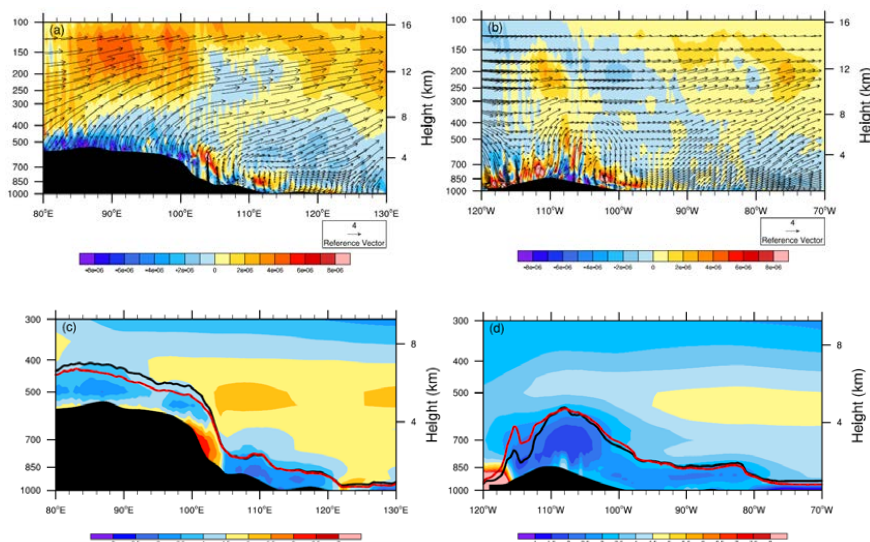
186

187

188   Figure 3. Vertical distribution of divergence (s^{-1}) (shaded) at the latitude across
189   sections from 30N to 35N in (a) East Asia, (b) North America. The vectors of daily U-
190   and W- wind components from 2010 to 2019 in summer along 30N–35N with the
191   zonal circulations. The black shaded area represents topography. The red and black
192   lines in Figure (c) and (d) denote the LCL and PBLH, respectively. The shaded colors
193   except black in Figure (c) and (d) represent the vertical gradients of virtual potential
194   temperature dθ_v/dz.
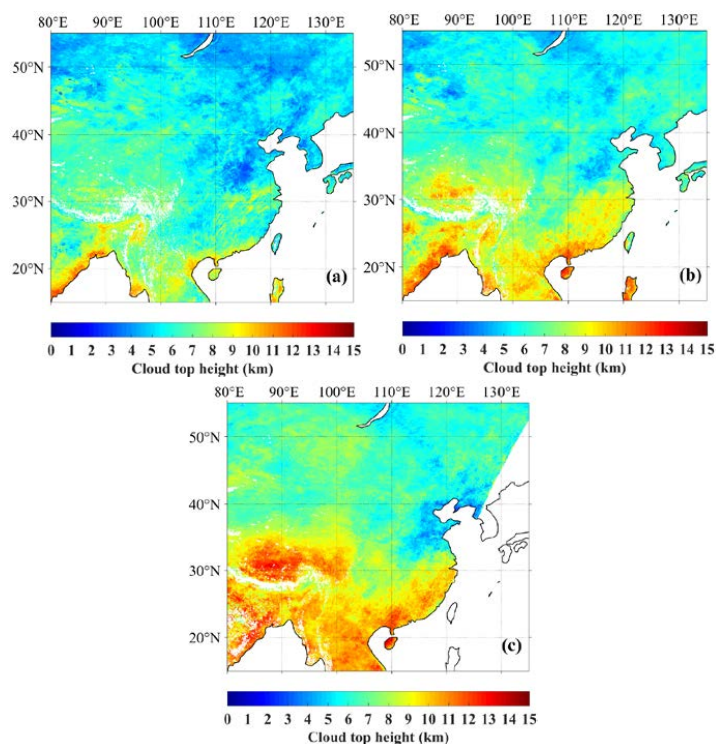
195

196

197 Figure 4. The median cloud top height derived from himawari-8 retrieval product at
198 three Beijing times: (a) 2:30 pm±0.5h (b) 4:30 pm±0.5h (c) 6:30 pm±0.5h from June
199 to August in 2016 over land in East Asia. Missing data are shaded in white color.

200

201   On the other hand, we note that, compared to   eastern China, there is no obvious
202 decrease trend for the LCC over the TP from late afternoon to evening as shown in
203 Figure 2. The Figure 3 (a) shows there are obvious large scale ascending motions
204 from near surface layer to upper troposphere over the TP, which correspond with the
205 convergence at 500 hPa and the divergence at 200 hPa. Figure 3 (c) shows there are
206 deep weak inversion layer (about 2 km with $d\theta_v/dz < 3$ K km^{-1}) and positive
207 PBLH-LCL over the TP. These results are consistent with the conclusions proposed
208 by Xu et al. (2014) and Wang et al. (2020). In contrast, Figure 3 (b) shows there are
209 only weak large scale ascending motions from near surface layer to middle
210 troposphere over the Rocky Mountains, while the large-scale subsidence on both sides
211 of the Rocky Mountains leads to strong inversion above PBL and lower RH in near
212 surface layer. The former restricts the growth of PBLH during the day, and the latter
213 leads to the increased LCL. Thus negative PBLH-LCL is identified on both sides of
214 the Rocky Mountains, especially for the western Rocky Mountain with strong
215 large-scale subsidence, as shown in Figure 3 (d). With its thermal structure, the TP
216 leads to dynamic processes of vapor transport, similar to the CISK mechanism of
217 tropical cyclones.

218   Figure 4 shows the spatial distribution of day time variations of cloud top height
219   in summer. Compared to   eastern China at the same latitude, the cloud top height has
220   a significant increase from 2:30 pm (~7 km) to 6:30 pm (~14 km) over the TP. The
221   cloud top height approaches the tropopause (~14 km) in the evening over the TP,
222   which implies the frequent deep convective clouds at this time. This result is
223   consistent with the observation of millimeter-wave radar in Naqu (Yi, 2016).

224   By comprehensively analyzing the second Tibet Plateau Experiment (TIPEX II)
225   sodar data, Xu et al. (2002) and Zhou et al. (2000) found that, with narrow upward
226   motion and time scale from 1.2 h to 1.5 h, the maximum upward motion of the
227   thermal turbulence was identified at the height of about 120 m above the surface, its
228   vertical speed up to 1 m s-1.They also found   symmetrical and wide downward
229   motion area on either side of the narrow upward motion zone. The question arises as
230   to whether there is a relationship between the formation and evolution of frequent
231   "pop-corn-like" convective clouds and micro-scale thermal turbulence in the
232   atmospheric convective boundary layer over the TP. Xu et al., (2012) speculate these
233   low clouds are probably initiated by strong thermal turbulence under low air density
234   condition. Compared to the low elevation in eastern China, the increased thermal
235   turbulence associated with low air density over the TP leads to the different
236   turbulence characteristics of CBL. The CBL is mainly driven by buoyancy heat flux,
237   and thermal turbulence with organized thermal plume is not totally random (Young,
238   1988a; Young, 1988b). The BT and ST over the TP are significantly greater than those
239   at the low elevation, which play key roles in the convective activities in lower
240   troposphere.

241   By using the statistical results from sodar data in the second Tibetan Plateau
242   Experiment for atmospheric sciences (TIPEX II), Zhou et al. (2000) calculated the BT
243   and ST at the height of 50 m under strong convection condition in Dangxiong (located
244   at central TP). The results indicate that the BT is comparable to ST. Both the
245   thermodynamic and dynamic processes have important influences on the convective
246   activities. Both the BT and ST in the surface layer in Dangxiong are almost an order
247   of magnitude   greater than those at low elevation given by Brummer (1985) in North
248   Sea and Weckwerthet et al. (1997) in Florida. Direct measurements from the Third
249   Tibetan Plateau Experiments (TIPEX III) also confirmed that surface buoyancy flux
250   over the TP is significantly larger than that in eastern China (Zhou, 2000; Wang et al.,
251   2016). Both the sodar data in TIPEX II and boundary layer tower data in TIPEX III
252   showed contributions of BT and ST to the turbulent kinetic energy in the lower
253   troposphere are larger over the TP than over the southeastern margin of the TP and the
254   low-altitude Chengdu Plain (Zhou, 2000; Wang et al., 2015). What is the relationship
255   between high frequent low cloud and the above physical quantities (e.g. turbulence
256   structure, temperature and humidity) under low air density condition over the TP? The
257   physical mechanism should be discussed and analyzed. In addition, at low elevation in
258   eastern China, the question arises as to whether or not the variations of PBLH and
259   LCL favor the formation and development of low clouds.

260   As shown in Figure 5 (a), compared to the low elevation, for low RH_{2m} condition
261   ($RH_{2m} < 40\%$), there is larger LCC (LCC > 50%) over the TP (AGL > 3 km). In

262   contrast, larger LCC mostly corresponds to   higher RH_{2m} condition at low elevation,
263   which is consisted with our common sense. The above interesting phenomenon can be
264   explained by the differences of PBLH-LCL between TP and low elevation on summer
265   afternoons, which are mainly attributed to two mechanisms. With a similar sensible
266   heat flux, the lower air density over the TP leads to greater surface buoyancy flux (or
267   BT) as shown in Figure 5 (c), which is conducive to the increase of   PBLH over the
268   TP. Figure 5 (d) shows great ST over the TP, which is mainly attributed to large wind
269   speed. Although here we only show the ST in surface layer, strong wind shear in
270   boundary layer probably also plays a role in increasing PBLH over the TP. On the
271   other hand, with a similar RH, Wang et al. (2020) have indicated that, compared to the
272   low elevation in eastern China, the lower temperature over the TP leads to a lower
273   LCL. Together these mechanisms lead to a greater (PBLH-LCL) difference over the
274   TP on summer afternoons, which increase the probability of air parcels reaching the
275   LCL and forming clouds as shown in Figure 5 (b).
276
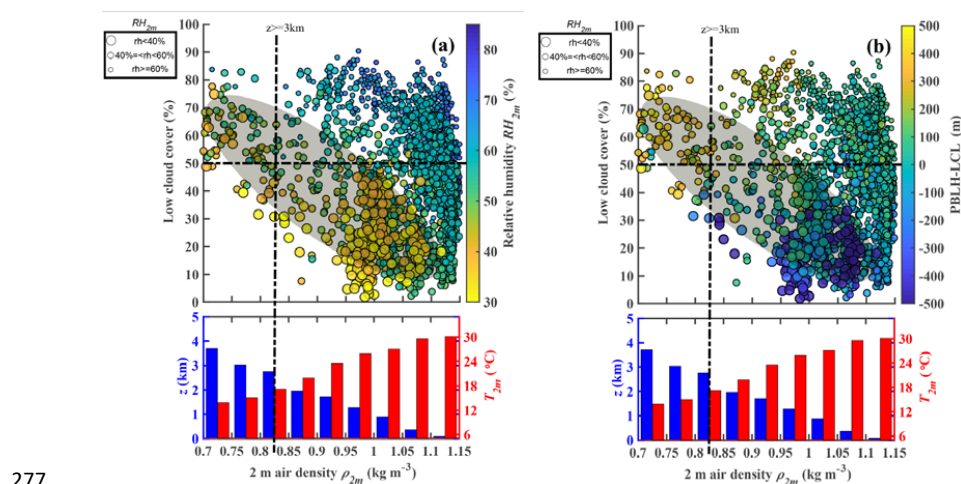
277
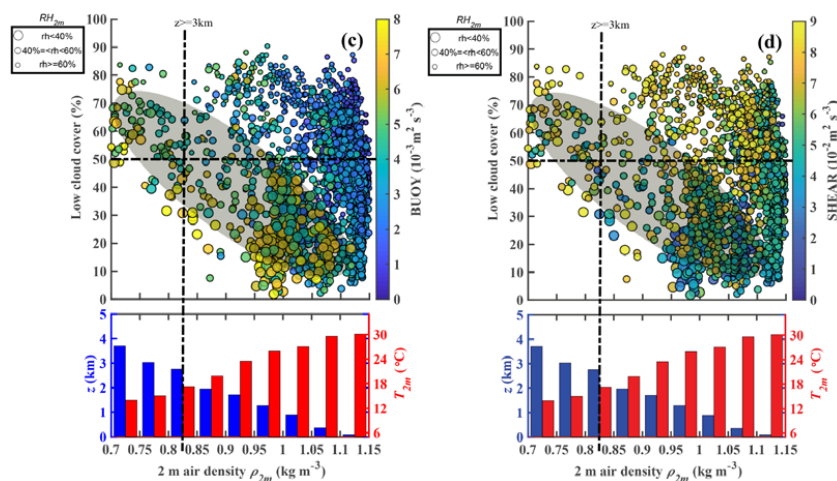
278

279 Figure 5. The relationships among monthly means of low cloud cover LCC, ρ_{2m} and
280 (a) RH_{2m}, (b) PBLH-LCL, (c) BT and (d) ST at 2:00 pm (BT) from 2010 to 2019 in
281 summer in China. The samples are divided into three groups: $RH_{2m} >= 60\%$ (small
282 size dots), $60\% > RH_{2m} >= 40\%$ (median size dots) and $RH_{2m} < 40\%$ (large size dots).
283 The LCC, T2m and RH2m are observed by in situ measurements, and PBLH, LCL,
284 BT and ST are derived from ERA5 reanalysis data. Here we use the nearest neighbor
285 gridding method to derive the PBLH, LCL, BT and ST at each site. The blue and red
286 histograms show an approximate relationship between ρ_{2m} and surface elevation
287 above sea level z, air temperature at 2 m (T_{2m}) at the bottom of Figure 1a, respectively.
288 The dots with lower RH_{2m} ($RH_{2m} < 40\%$) are mostly distributed within grey shaded
289 elliptic region as shown in Figure 5 (a)-(d).

290   Based on the spatial distribution of topography in the northern hemisphere as
291 shown in Figure 6 (a), it is clear that both the TP and Rocky Mountains in North
292 America are typical large topography regions. From the viewpoint of global effects,
293 the triggering effects of dynamical structure within the boundary layer on convective
294 clouds in the northern hemisphere are discussed. Figure 6 (d) shows the mean spatial
295 distribution of PBLH – LCL in the northern hemisphere from June to August of
296 2010-2019. The TP and Rocky Mountains are two typical high value regions in the
297 northern hemisphere, and the mean PBLH – LCL over the TP and Rocky Mountains
298 are 376.7 m and -101.9 m, respectively.

299   Figure 6 (b)-(c) show the spatial distribution of ST and BT in the northern
300 hemisphere from June to August of 2010-2019, respectively. The effect of strong
301 thermal turbulence results in obvious positive value of PBLH – LCL at high elevation
302 regions under low air density condition in the northern hemisphere (BT = 0.008 m^2 s^{-3},
303 PBLH – LCL = 376.7 m over the TP and BT = 0.011 m^2 s^{-3}, PBLH – LCL = -101.9 m
304 over the Rocky Mountains). Figure 6 (b) also shows that there are strong STs at these
305 two high elevation regions (ST = 0.087 m^2 s^{-3} over the TP and ST = 0.085 m^2 s^{-3} over
306 the Rocky Mountains). Both the BT and ST increase significantly at high elevation
307 due to low air density compared to those at low elevation. The above results enlighten
308 us on thinking about whether the triggering effects of large topography and
309 boundary layer turbulence, which reflect the special turbulence characteristics in
310 boundary layer at high elevation regions under low air density condition, can be
311 applicable for any large topography in the globe, including TP and other regions (e.g.
312 Rocky Mountains).

313   Figure 7 shows the conceptual model of atmosphere from the near-surface to
314 upper troposphere over the TP. Compared to the low elevation, the TP is characterized
315 by higher PBLH and lower LCL because of strong BT and ST, which is favorable for
316 the formation of shallow clouds in the afternoon. Meanwhile, the large scale
317 ascending motion over the TP results in the transition from shallow clouds to deep
318 convective clouds in the late afternoon and evening.

319

320

321

322

323
324

325
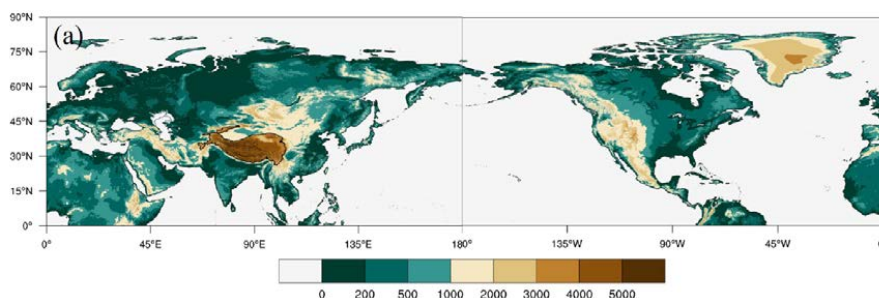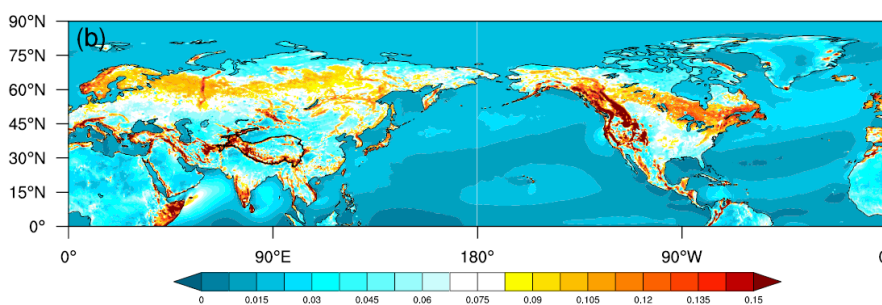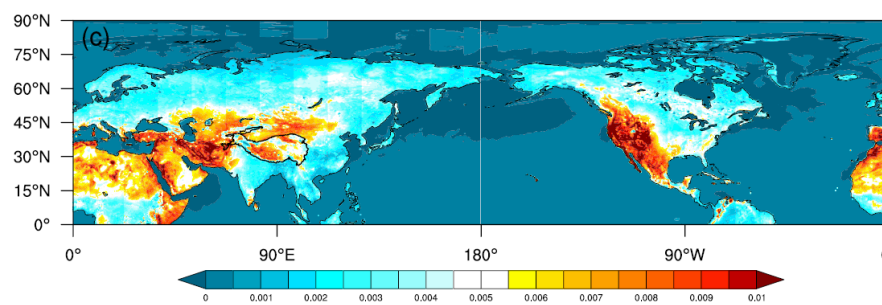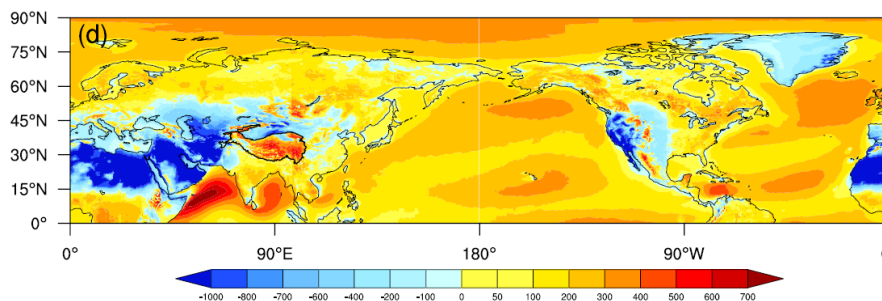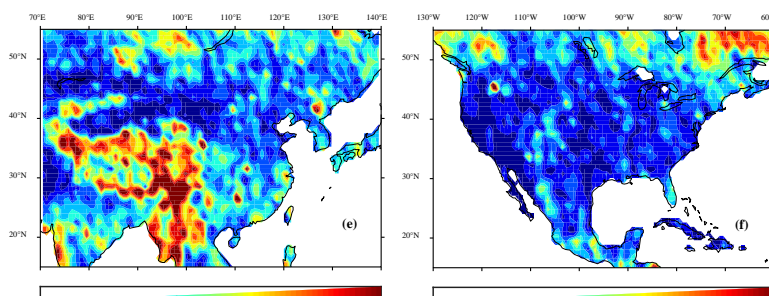
Figure 6. The spatial distribution of (a) AGL, (b) ST, (c) BT, (d) PBLH-LCL, and (e)
LCC derived from cloudsat satellite data at local time 2:00 pm in the Northern
Hemisphere in summer.

329
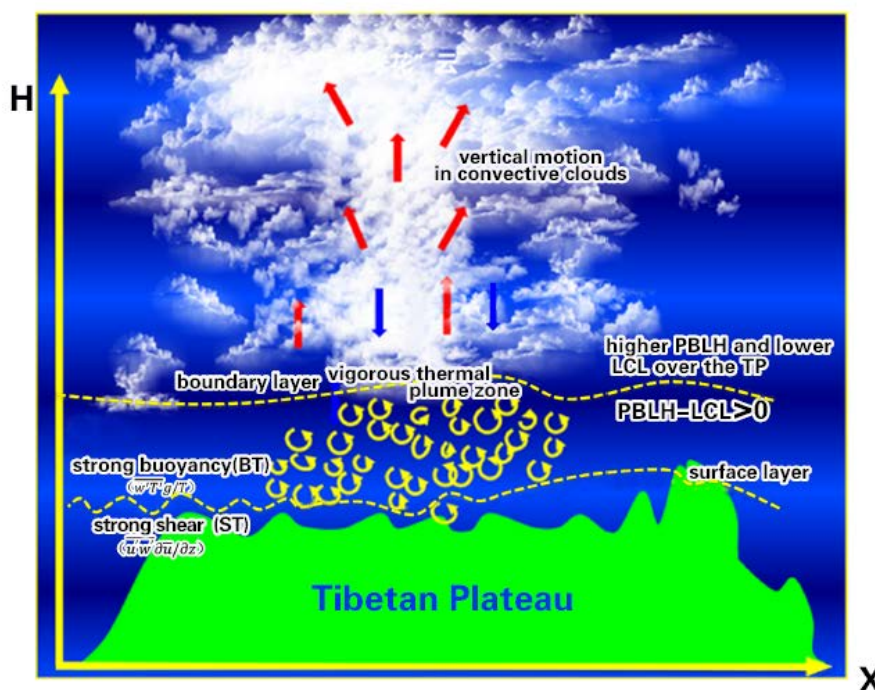
Figure 7. The characteristics model of boundary layer turbulence related to "high
efficiency" triggering mechanisms for convection over the TP.

4 Conclusions and further discussion

In this study, we focus on the triggering effects of large topography and
boundary layer turbulence over the Tibetan Plateau on convection. The topography of
TP also has a major role in the increasing of occurrences of convective clouds. Our

336 results further confirm the conclusions from Wang et al. (2020), which found that
337 PBLH-LCL over the TP is greater than that in eastern China. Compared to the eastern
338 China, with the same relative humidity, lower temperature over the TP results in a
339 lower lifting condensation level. With the same surface sensible heat flux, lower air
340 density over the TP results in a larger buoyancy flux and a deeper boundary layer. The
341 observational results show that, under low relative humidity condition (RH < 40%),
342 the low cloud cover (LCC) is higher than 60%   over the TP. In contrast, the high
343 LCC (LCC > 60%) only appears under conditions with high RH (RH > 60%) at low
344 elevation.

345   In general, LCC increases with the increasing elevation. The median of LCCs at
346 high elevation (TP) are significantly greater than those at low elevation (eastern China)
347 throughout the day. The diurnal variations of LCC in eastern China are generally
348 distributed in unimodal pattern with the maximum appearing at 2:00 pm BT and   low
349 values during the night. The diurnal variations of LCC at high elevation (TP) present
350 a bimodal curve with the maximum appearing at 5:00 pm BT and the secondary local
351 maximum appearing at 8:00 am BT. In addition, LCC maintains at high values at high
352 elevation (TP) during the day. The median cloud top height derived from himawari-8
353 retrieval product shows the transition from shallow clouds to deep convective clouds
354 in the late afternoon and evening over the TP, which is attributed to the strong
355 large-scale ascending motion from the near surface to upper troposphere over the TP.

356   The buoyancy term (BT) and shear term (ST) over the TP are significantly greater
357 than those at the low elevation, which is favorable for the formation of increasing
358 PBLH. Similar phenomenon occurs at other high elevation area (e.g. Rocky
359 Mountains). The strong thermal turbulence results in positive value of PBLH-LCL at
360 high elevation regions under low RH condition in the northern hemisphere. The
361 slightly greater than zero   PBLH-LCL corresponds spatially to more LCC in the
362 central part of Rocky Mountains, but obvious large-scale subsidence on both sides of
363 the mountain leads to strong inversion above PBL and lower RH in PBL, which
364 further lead to less LCC in these areas. Thus   less LCC is generated at Rocky
365 Mountains compared to the TP.

366

Data availability

368 All reanalysis data used in this study were obtained from publicly available sources:
369 ERA5 reanalysis data can be obtained from the ECMWF public datasets web interface
370 (http://apps.ecmwf.int/datasets/). The satellite (CloudSat radar and Calipso
371 lidar)-merged cloud classification product 2B-CLDCLASS-lidar were obtained from
372 Colorado   State   University
373 (http://www.cloudsat.cira.colostate.edu/data-products/level-2b/2b-cldclass-lidar). The
374 himawari-8 retrieval products were obtained from JAXA Himawari Monitor
375 (https://www.eorc.jaxa.jp/ptree/).

Code Availability

The data in this study are analysed with MATLAB. Contact Y.W. for specific code

requests.

Acknowledgements

Xu and Wang are supported by the Second Tibetan Plateau Scientific Expedition and
Research (STEP) program (Grant Nos. 2019QZKK0105), National Natural Science
Foundation of China (Grant Nos. 91837310), and the National Natural Science
Foundation for Young Scientists of China (Grant Nos. 41805006).

Author Contributions

X.X. and Y. W. led this work with contributions from all authors. Y.T. and Y. W.
made the calculations and created the figures. X.X, Y.W. and S.Z. led analyses,
interpreted results and wrote the paper.

Competing interests

The authors declare no competing interests.

References

Brümmer, B.: Structure, dynamics and energetics of boundary layer rolls from Kon
Tur aircraft observations, undefined, 1985.

Dyer, A. J.: A review of flux-profile relationships, Bound.-Layer Meteorol., 7, 363–
372, https://doi.org/10.1007/bf00240838, 1974.

Ek, M. and Mahrt, L.: Daytime Evolution of Relative Humidity at the Boundary
Layer Top, Mon. Weather Rev., 122, 2709–2721,
https://doi.org/10.1175/1520-0493(1994)122<2709:DEORHA>2.0.CO;2, 1994.

Findell, K. L. and Eltahir, E. A. B.: Atmospheric Controls on Soil Moisture–Boundary
Layer Interactions. Part I: Framework Development, J. Hydrometeorol., 4, 552–569,
https://doi.org/10.1175/1525-7541(2003)004<0552:ACOSML>2.0.CO;2, 2003.

Flohn, H. and Reiter, E. R.: Contributions to a meteorology of the Tibetan highlands,
1967.

Gentine, P., Holtslag, A. A. M., D'Andrea, F., and Ek, M.: Surface and Atmospheric
Controls on the Onset of Moist Convection over Land, J. Hydrometeorol., 14, 1443–
1462, https://doi.org/10.1175/JHM-D-12-0137.1, 2013.

Guillod, B. P., Orlowsky, B., Miralles, D. G., Teuling, A. J., and Seneviratne, S. I.:

411   Reconciling spatial and temporal soil moisture effects on afternoon rainfall, Nat.
412   Commun., 6, 6443, https://doi.org/10.1038/ncomms7443, 2015.

413   Hersbach, H., Bell, B., Berrisford, P., Hirahara, S., Horányi, A., Muñoz-Sabater, J.,
414   Nicolas, J., Peubey, C., Radu, R., Schepers, D., Simmons, A., Soci, C., Abdalla, S.,
415   Abellan, X., Balsamo, G., Bechtold, P., Biavati, G., Bidlot, J., Bonavita, M., Chiara, G.
416   D., Dahlgren, P., Dee, D., Diamantakis, M., Dragani, R., Flemming, J., Forbes, R.,
417   Fuentes, M., Geer, A., Haimberger, L., Healy, S., Hogan, R. J., Hólm, E., Janisková,
418   M., Keeley, S., Laloyaux, P., Lopez, P., Lupu, C., Radnoti, G., Rosnay, P. de, Rozum,
419   I., Vamborg, F., Villaume, S., and Thépaut, J.-N.: The ERA5 global reanalysis, Q. J. R.
420   Meteorol. Soc., 146, 1999–2049, https://doi.org/10.1002/qj.3803, 2020.

421   Li, Y. and Zhang, M.: Cumulus over the Tibetan Plateau in the Summer Based on
422   CloudSat–CALIPSO Data, J. Clim., 29, 1219–1230,
423   https://doi.org/10.1175/JCLI-D-15-0492.1, 2016.

424   Luo, Y., Zhang, R., Qian, W., Luo, Z., and Hu, X.: Intercomparison of Deep
425   Convection over the Tibetan Plateau–Asian Monsoon Region and Subtropical North
426   America in Boreal Summer Using CloudSat/CALIPSO Data, J. Clim., 24, 2164–2177,
427   https://doi.org/10.1175/2010JCLI4032.1, 2011.

428   Sassen, K. and Wang, Z.: Classifying clouds around the globe with the CloudSat radar:
429   1-year of results, Geophys. Res. Lett., 35, https://doi.org/10.1029/2007GL032591,
430   2008.

431   Stull, R. B.: Mean Boundary Layer Characteristics, in: An Introduction to Boundary
432   Layer Meteorology, edited by: Stull, R. B., Springer Netherlands, Dordrecht, 1–27,
433   https://doi.org/10.1007/978-94-009-3027-8_1, 1988.

434   Sugimoto, S. and Ueno, K.: Role of Mesoscale Convective Systems Developed
435   around the Eastern Tibetan Plateau in the Eastward Expansion of an Upper
436   Tropospheric High during the Monsoon Season, J. Meteorol. Soc. Jpn. Ser II, 90,
437   297–310, https://doi.org/10.2151/jmsj.2012-209, 2012.

438   Taylor, C. M., de Jeu, R. A. M., Guichard, F., Harris, P. P., and Dorigo, W. A.:
439   Afternoon rain more likely over drier soils, Nature, 489, 423–426,
440   https://doi.org/10.1038/nature11377, 2012.

441   Tuttle, S. and Salvucci, G.: Empirical evidence of contrasting soil moisture–
442   precipitation feedbacks across the United States, Science, 352, 825–828,
443   https://doi.org/10.1126/science.aaa7185, 2016.

444   Wang, Y., Xu, X., Zhao, T., Sun, J., Yao, W., and Zhou, M.: Structures of convection
445   and turbulent kinetic energy in boundary layer over the southeastern edge of the
446   Tibetan Plateau, Sci. China Earth Sci., 58, 1198–1209,
447   https://doi.org/10.1007/s11430-015-5054-1, 2015.

Wang, Y., Xu, X., Liu, H., Li, Y., Li, Y., Hu, Z., Gao, X., Ma, Y., Sun, J., Lenschow, D. H., Zhong, S., Zhou, M., Bian, X., and Zhao, P.: Analysis of land surface parameters and turbulence characteristics over the Tibetan Plateau and surrounding region, J. Geophys. Res. Atmospheres, 121, 9540–9560, https://doi.org/10.1002/2016JD025401, 2016.

Wang, Y., Zeng, X., Xu, X., Welty, J., Lenschow, D. H., Zhou, M., and Zhao, Y.: Why Are There More Summer Afternoon Low Clouds Over the Tibetan Plateau Compared to Eastern China?, Geophys. Res. Lett., 47, e2020GL089665, https://doi.org/10.1029/2020GL089665, 2020.

Weckwerth, T. M., Wilson, J., Wakimoto, R., and Crook, N. A.: Horizontal convective rolls: Determining the environmental conditions supporting their existence and characteristics, Mon. Weather Rev., 125, 505–526, https://doi.org/10.1175/1520-0493(1997)12560;0505:hcrdte62;2.0.co;2, 1997.

Wu, G., Duan, A., Liu, Y., Mao, J., Ren, R., Bao, Q., He, B., Liu, B., and Hu, W.: Tibetan Plateau climate dynamics: recent research progress and outlook, Natl. Sci. Rev., 2, 100–116, https://doi.org/10.1093/nsr/nwu045, 2015.

Xu, X., Zhou, M., Chen, J., Bian, L., Zhang, G., Liu, H., Li, S., Zhang, H., Zhao, Y., Suolongduoji, and Jizhi, W.: A comprehensive physical pattern of land-air dynamic and thermal structure on the Qinghai-Xizang Plateau, Sci. China Ser. D, 45, 577–594, https://doi.org/10.1360/02yd9060, 2002.

Xu, X., Zhang, R., Koike, T., Lu, C., Shi, X., Zhang, S., Bian, L., Cheng, X., Li, P., and Ding, G.: A New Integrated Observational System Over the Tibetan Plateau, Bull. Am. Meteorol. Soc. - BULL AMER METEOROL SOC, 89, 1492–1496, https://doi.org/10.1175/2008BAMS2557.1, 2008.

Xu, X., Shi, X., and Lu, C.: Theory and application for warning and prediction of disastrous weather downstream from the Tibetan Plateau, Theory Appl. Warn. Predict. Disastrous Weather Downstr. Tibet. Plateau, 1–116, 2012.

Xu, X., Zhao, T., Lu, C., Guo, Y., Chen, B., Liu, R., Li, Y., and Shi, X.: An important mechanism sustaining the atmospheric "water tower" over the Tibetan Plateau, Atmospheric Chem. Phys., 14, 11287–11295, https://doi.org/10.5194/acp-14-11287-2014, 2014.

Yi, C., and Guo, X.: Characteristics of convective cloud and precipitation during summer time at Naqu over Tibetan Plateau (in Chinese), Chinese Science Bulletin, 61, 1706–471, https://doi.org/10.1360/N972015-01292, 2016.

Young, G. S.: Convection in the atmospheric boundary layer, Earth-Sci. Rev., 25, 179–198, https://doi.org/10.1016/0012-8252(88)90020-7, 1988a.

Young, G. S.: Turbulence Structure of the Convective Boundary Layer. Part I.

485   Variability of Normalized Turbulence Statistics, J. Atmospheric Sci., 45, 719–726,

486   https://doi.org/10.1175/1520-0469(1988)045<0719:TSOTCB>2.0.CO;2, 1988b.

487   Zhou, M., Xu, X., Bian, L., Chen, J., Liu H., Zhang, H., Li, S., and Zhao J.:

488   Observational analysis and dynamic study of atmospheric boundary layer on Tibetan

489   Plateau (in Chinese), 125 pp., 2000.

490